21st AIAA Computational Fluid Dynamics Conference
June 24-27, 2013, San Diego, CA
AIAA 2013-2445

Boundary Layer Adaptivity for Transonic Turbulent Flows

Kedar C. Chitale*
University of Colorado Boulder, Boulder, CO, 80309-0429

Onkar Sahni†
Rensselaer Polytechnic Institute, Troy, NY, 12180-3590

Saurabh Tendulkar and Rocco Nastasia
Simmetrix Inc., Clifton Park, NY, 12065

Mark S. Shephard‡
Rensselaer Polytechnic Institute, Troy, NY, 12180-3590

Kenneth E. Jansen§
University of Colorado Boulder, Boulder, CO, 80309-0429

Simulations of turbulent flows are challenging and require tight and varying mesh spacings near the walls that depend on the turbulence models used. Semi-structured meshes are often used in the turbulent wall boundary layers due to their ability to be strongly graded and anisotropic. To reduce the discretization errors in the solution, an adaptive approach becomes essential due to the lack of good *a priori* error indicators. Properties of the turbulent boundary layers can be directly calculated from the flow physics and can be used to guide adaptivity. This paper introduces a new approach for adaptivity of the mesh boundary layers using flow physics indicators, in combination with classical numerical error indicators. The effectiveness of the adaptive techniques is analyzed by applying them to transonic flow problems with shock wave and boundary layer interactions.

Nomenclature

ρ	Density, kg/m^3
P_t, T_t	Stagnation pressure, Pa and stagnation temperature, K
τ_w	Wall shear stress
u_τ	Friction velocity, m/s
μ	Absolute viscosity, $kg.m/s$
ν	Kinematic viscosity, m^2/s
y^+	Dimensionless distance from the wall $(\rho u_\tau y/\mu)$
u^+	Dimensionless velocity (u/u_τ)
δ_{99}	Velocity boundary layer thickness
C_p	Coefficient of pressure
a	Speed of sound
b	Span of the wing
$clocal$	local cord of the section

*PhD candidate, University of Colorado Boulder, AIAA Student Member, Tel.: +1-518-596-4750
†Assistant Professor, Rensselaer Polytechnic Institute
‡Professor, Rensselaer Polytechnic Institute, Tel.: +1-518-276-8044
§Professor, University of Colorado Boulder, Tel.: +1-303-492-4359

I. Introduction

The accuracy of CFD simulations strongly depends on the mesh resolution and quality. In complex flow problems, it is difficult to determine the adequate mesh resolution *a priori*. In such cases, an initial mesh is used to get a first estimate of the flow solution, and the mesh is adapted using *a posteriori* error indicators. In order to expedite the numerical computations, the resolution needs to be applied in a local fashion, which can be achieved by locally modifying the mesh elements, based on a size field. Traditionally, scalar error indicators have been used to calculate the size field, leading to isotropic elements. But most flow problems of interest exhibit highly anisotropic features such as boundary layers, shear layers, shock waves etc. These features are most efficiently resolved with anisotropic elements, i.e. elements oriented and stretched in a certain manner.

For viscous flows, boundary layers are a prominent flow feature and need to be resolved accurately. Moreover, if the boundary layers are turbulent, which is often the case for high Reynolds number flows, mesh spacings in this region need to be very fine. Using isotropic elements here puts excessive demands on the computational resources due to extreme increase in the size of the mesh. Using fully unstructured anisotropic elements creates poorly shaped elements, which may cause problems for the flow solver. To remedy these problems, layered, orthogonal and graded mesh elements, called *mesh boundary layers* of a given thickness are used near the no-slip walls and the rest of the flow region is meshed with unstructured elements. A common method to construct these meshes is *advancing layers method*.[1,2] During adaptivity, it is desirable to maintain this advantageous layered structure of elements. Mesh adaptation procedures have been implemented for mesh boundary layers,[3] and recently have been extended to parallel systems.[4] However, application of these procedures to highly turbulent and high speed flows is still a topic of research.

Turbulent boundary layers have been studied extensively, both experimentally and computationally, and the resolution requirements near the walls are well understood for different modeling approaches.[5–8] These resolution requirements are usually defined with a dimensionless distance (y^+) and vary according to the modeling methods (RANS, LES, DNS) and the type of wall treatment (resolved, modeled). Since the mesh spacing requirements in the boundary layer region largely depend on the flow physics, it is advantageous to use this insight to drive the adaptivity, locally. Moreover, high speed flows pose a greater challenge in the regions where shock waves and boundary layers interact. The mesh sizes in these regions need to be carefully chosen.

This paper focuses on thickness adaptation of mesh boundary layers based on the knowledge of the turbulence model used for the simulations and the flow physics of the boundary layers. Algorithms are outlined to set the mesh attributes in the boundary layers based on the physics of attached boundary layers. Special strategies for detection and adaptivity of regions like separated boundary layers and shock wave - boundary layer interaction zones are discussed.

The article is organized as follows. Section II describes anisotropic adaptivity techniques and how they are extended to boundary layer meshes. Section III outlines the new strategies that we have developed to calculate thickness specifications of the mesh within the boundary layers. Section IV illustrates the capability of our approach by showcasing results of two transonic flow applications.

II. Anisotropic adaptivity and boundary layers

Boundary layer meshes are widely used in simulations of the turbulent flows. These semi-structured meshes provide an easy way to achieve elements with anisotropy of 10,000 or more, without creating poorly shaped elements with extremely large dihedral angles which would severely influence the flow resolution, at least locally. Fig. 1 shows an example of a boundary layer mesh for a simple pipe geometry.[4] For 3-D meshes, boundary layer meshes are comprised of prisms and pyramids, whereas the unstructured region is meshed with tetrahedra.

The important parameters of the mesh boundary layers are:

1. First cell height (Distance of the first mesh point from the wall surface) (t_o)
2. Total height of the mesh boundary layer (T)
3. Total number of layered elements (n)
4. Growth factor(r)

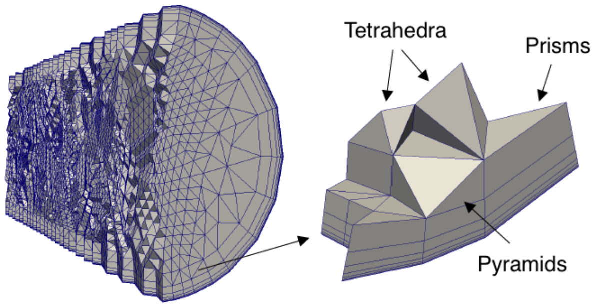

Figure 1. Mesh boundary layers for a pipe geometry

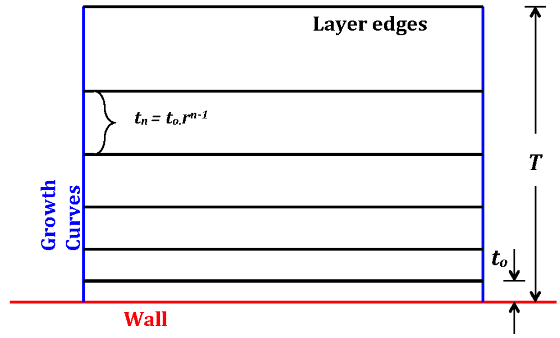

Figure 2. A 2D sketch of the boundary layer mesh

The interdependence of these parameters is given by the following equation:

$$T = t_o \sum_{i=1}^{i=n} r^{(i-1)} \tag{1}$$

The growth factor is the multiplication factor by which the height of every succeeding element increases with respect to the previous element in that layer, away from the wall. Three of the above parameters can be chosen independently, and the fourth one is determined through eq. 1. Fig. 2 shows the general structure of a boundary layer mesh viewed in 2D and shows some of the key attributes of these meshes. Out of these, t_o and T are physically the most important. As described in section III, we use flow physics information from the boundary layer to set these parameters. The in-plane resolution of the boundary layers and the mesh sizes in the unstructured region, are controlled by the numerical error indicators, which are explained next.

A. Hessian driven adaptivity

Outside the boundary layer, the mesh can also be anisotropic. Since the level of anisotropy required outside the boundary layer is much less, general unstructured anisotropic meshes are used and the mesh anisotropy is defined using the well known Hessian based methods.[9,10] The anisotropic adaptivity used in this work, is based on the local modifications of the mesh elements following a *mesh metric field*.[11] The mesh metric is derived from a Hessian, which is a symmetric matrix constructed from the second derivatives of the flow solution variables. Traditionally speed and density are chosen as the solution variables, but a combination of different variables can also be used. It is possible to obtain local estimates of the interpolation error in different norms, based on the Hessian.[12]

The Hessian matrix is decomposed as $H = R\Lambda R^T$, where R is the matrix of eigenvectors and Λ is the diagonal matrix of eigenvalues. The directions associated with the eigenvectors are referred to as the principal directions and the eigenvalues are equivalent to the second derivatives along these directions. High eigenvalues are associated with high error in the corresponding direction. Similarly, a low eigenvalue means lower error in the corresponding direction.[13] Mesh sizes (mesh edge lengths in particular directions) can be calculated as scaled inverses of the eigenvalues at each vertex of the mesh.

The mesh metric field can be thought of as a transformation matrix which defines a mapping of an ellipsoid in the physical space into a unit sphere in the metric space, as shown in fig. 3. An element of any shape in the physical space is transformed to an equilateral element in the metric space with this transformation.

The mathematical form of this transformation matrix is given by eq. 2:

$$\boldsymbol{T(x,y,z)} = \begin{bmatrix} 1/h_1 & 0 & 0 \\ 0 & 1/h_2 & 0 \\ 0 & 0 & 1/h_3 \end{bmatrix} \begin{bmatrix} \vec{e_1} \\ \vec{e_2} \\ \vec{e_3} \end{bmatrix} \tag{2}$$

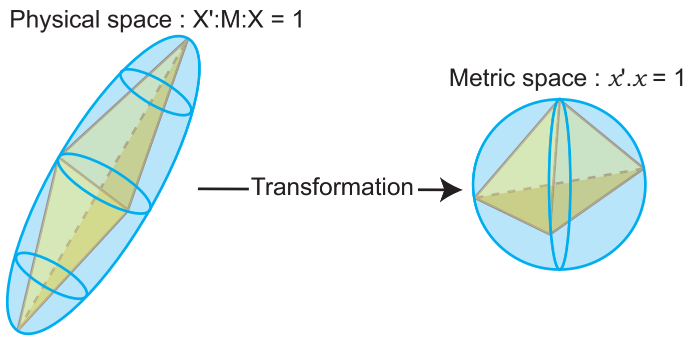

Figure 3. Transformation associated with the mesh metric tensor[3]

where $\overrightarrow{e_1}, \overrightarrow{e_2}, \overrightarrow{e_3}$ are the unit vectors in the three principal directions and h_1, h_2, h_3 are the desired mesh edge lengths (mesh sizes) in the corresponding directions. The goal of the adaptation software is to achieve unit edge lengths in the metric space. This criteria is usually relaxed to ensure a mesh can be obtained.

1. Extension to boundary layers

The methodology outlined above works well for unstructured elements. When working with boundary layers we want to preserve their structured nature, and using this technique directly does not guarantee that. To extend anisotropic adaptivity to boundary layer meshes, following approach is used.

Fig. 4(a) shows a conceptual decomposition of the boundary layer mesh. The boundary layer meshes can be viewed as a product of a layer surface (2D) and a thickness (1D) mesh. The lines which are roughly orthogonal to the wall are referred to as the *growth curves*, and the triangular surfaces parallel to the wall are referred to as the *layer surfaces*. Each layer of elements is formed with the help of the layer surfaces above and below, connected by the growth edges in between. The mesh sizes on the layer surfaces are referred to as the *in-plane* sizes and the ones on the growth curves are referred to as the *normal* spacings. The ellipsoid in fig. 3 can be decomposed as an ellipse lying on the layer surfaces and a normal component aligned with the growth curves. This concept is shown in fig. 4(b).

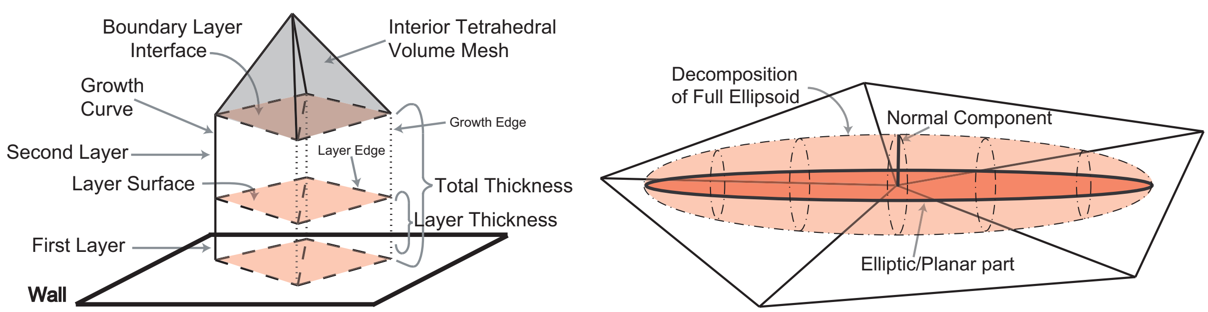

(a) Decomposition of the boundary layer mesh (b) Decomposition of the ellipsoid

Figure 4. Conceptual extension of the Hessian approach to boundary layers[3]

Adaptivity is carried out in two stages; *in-plane adaptation* achieves the required mesh sizes on the layer surfaces and does not affect the thickness, and *thickness adaptation* changes the normal spacing of the boundary layers. The in-plane adaptation is driven by the Hessian driven mesh metric field as described in this section (see Sahni et al.[3,13] and Ovcharenko et al.[4]). The thickness adaptation is driven by the procedures outlined in the next section.

III. Thickness Adaptation

To efficiently resolve the boundary layers in turbulent flows, careful control of the distribution of points normal to the wall is critical. The Hessians tend to be less accurate near the walls and therefore they are not a good candidate to drive thickness adaptation for such a critical flow region. Since, the mesh spacings in this region are largely dictated by the flow physics and the turbulence model being used, it makes more sense to use this information for thickness adaptation instead.

To demonstrate how critical the point distribution normal to the wall can be for turbulent flows, fig. 5 shows boundary layer profiles for a turbulent pipe flow, varying the first cell height from y^+ of 1 to 10. The results start showing wrong boundary layer profile for $y^+ > 5$, with worst profile obtained with no boundary layer mesh. These results were obtained with RANS Spalart Allmaras (RANS-SA)[14] turbulence model with wall resolved approach. The behavior would be different for other turbulence models and for the wall modeling approach.

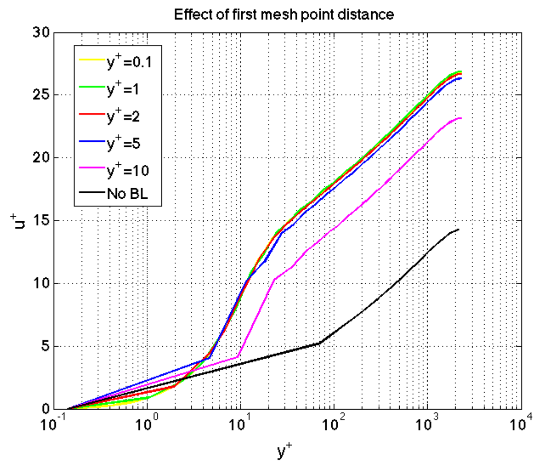

Figure 5. Effect of the first cell height on a turbulent boundary layer profile (RANS Spalart Allmaras (RANS-SA) turbulence model)

A. Types of boundary layers

At this point it is important to define the different classes of boundary layers, as control of the mesh parameters is different for each one. The boundary layers are usually classified into laminar boundary layers and turbulent boundary layers. However, this paper focuses on turbulent boundary layers as they are the most prevalent type for high Reynolds number flows and are much more complex in nature. Also, the mesh spacing requirements to resolve the turbulent boundary layers are much tighter than that for the laminar boundary layers, due to much larger velocity gradients near the wall (fig. 6). Thus our treatment for turbulent boundary layers is sufficient for resolving laminar boundary layers as well.

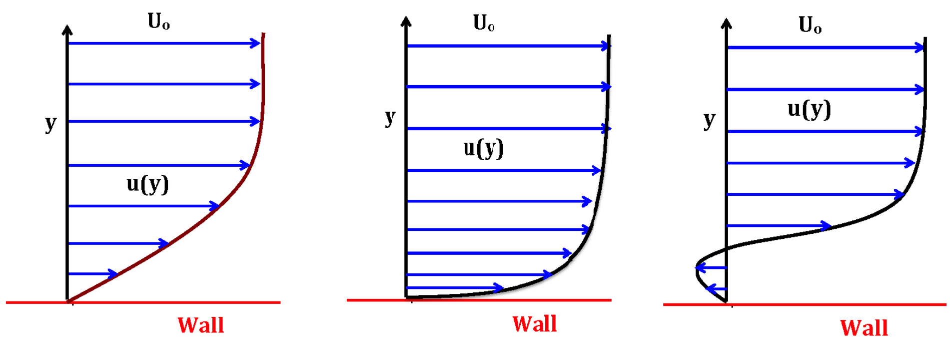

(a) Laminar BL (b) Turbulent BL (c) Separated BL

Figure 6. Types of boundary layer profiles

The second classification of the boundary layers relates to if the boundary layer is attached or separated. In many flows, due to adverse pressure gradients, boundary layers separate from the wall and form a free shear layer. The treatment of separated boundary layers needs special care as the flow physics in this region is entirely different than that of the attached boundary layers. Fig. 6 shows the two types of attached boundary layer profiles and a typical separated boundary layer profile.

B. Calculation of the wall shear stress

The near wall mesh spacing requirements for turbulent models depend on y^+, which needs the knowledge of the friction velocity u_τ, which can be calculated from the wall shear stress τ_w as $u_\tau = \sqrt{\frac{\tau_w}{\rho}}$. Many solvers readily provide wall shear stress as a field after post processing. However, we use alternative methods to calculate this field in a fast and an efficient manner.

Since most of the boundary layers in high Reynolds number flows are turbulent, one method to calculate τ_w is by using the Spalding's law. It gives y^+ as a function of u^+, written in a special form given by:[15]

$$y^+ = f(u^+) = u^+ + A[e^{(\kappa u^+)} - 1 - (\kappa u^+)^2/2 - (\kappa u^+)^3/6 - (\kappa u^+)^4/24] \tag{3}$$

where $A = 0.1108$ and $\kappa = 0.4$ are dimensionless constants. This law is valid through the entire turbulent boundary layer profile. u^+ is the dimensionless velocity at points along an attached boundary layer, normalized by the friction velocity (u/u_τ).

Using eq. 3, u^+ can be calculated at various points along the boundary layer, with following iterative approach.

1. Calculate the distance of the point on the boundary layer from the wall: Δy.
2. Retrieve the velocity at this point from the flow solution: u.
3. Guess an initial value of u_τ^1 and calculate initial $u^+ = u/u_\tau^1$ and $y^+ = \Delta y u_\tau^1/\nu$.
4. Use Newton's method to iteratively solve eq. 3 till convergence and update value of u_τ at each iteration.
5. Use the final value of u_τ to calculate the final value of u^+ (u/u_τ).

This process can be repeated at any number of points along the boundary layer. In the end, a simple average over the number of points used gives the final friction velocity u_τ. We use 3 to 5 points on an average along the growth curves, to calculate a more globally smooth u_τ. The wall shear stress can then be calculated as $\tau_w = u_\tau^2 \rho$.

Another method to calculate a quick and an approximate estimate of the wall shear stress, is using a finite difference approach near the wall. Using the first vertex from the wall and known u and Δy values at that point, τ_w can be calculated using $\tau_w = \mu \frac{du}{dy} = \mu \frac{u}{\Delta y}$. Here du equals u because the velocity is zero at the walls. This alternative method is used for flow regions where the boundary layers are not attached to the walls and Spalding's law is not applicable.

C. First cell layer height (t_o)

As already pointed out, different turbulence modeling approaches have different mesh spacing requirements close to the walls. Even in the same family of turbulence models like RANS, different approaches require varying mesh spacings depending on if the boundary layer is integrated to the wall (wall resolved approach) or if wall functions are used (wall modeling approach). The wall resolved approach makes a low Reynolds number assumption near the walls and requires that the first cell height is inside the viscous sub layer of the boundary layer ($y^+ < 5$). The wall modeling approach makes suitable assumptions for near wall behavior of the boundary layer and requires that the first cell height is beyond the viscous sub layer and into the log layer ($y^+ > 30$). If these requirements are not met for either of these modeling classes, then large numerical errors are possible in turbulence calculations predicting erroneous behavior, as seen in fig. 5. However, the friction velocity, which is required to calculate y^+, is not known *a priori*. This makes adaptive control of the first cell height very important.

Let us assume that the turbulence model requires first cell height to be equal to y_k^+. If we have an initial coarse mesh with a solution, using the wall shear stress (τ_w), t_o can be calculated, by the following algorithm:

1. Get the kinematic viscosity (ν) and desired y_k^+ according to the turbulence model from the user (Suggested values are $y_k^+ = 1$ for wall resolved RANS-SA, $y_k^+ = 30 - 50$ for wall modeled $k - \epsilon$, 0.5 for wall resolved $k - \epsilon$ etc.)
2. Calculate the friction velocity u_τ as discussed in the previous subsection.
3. Calculate the first layer height of the boundary layer by $t_o = \nu y_k^+/u_\tau$.

D. Total height of the boundary layer (T)

It is desirable to have the total height of the mesh boundary layers equal to or greater than the velocity boundary layer height given by δ_{99}. δ_{99} is the distance from the wall at which the velocity becomes 99% of the free stream velocity, and is an accepted measure of the boundary layer thickness. It is usually tricky to calculate δ_{99} directly as it requires knowledge of a reference velocity. For simple problems like a flat plate, the reference velocity is usually the free stream velocity, but it can have different local values for more complex problems, where the flow as a whole undergoes acceleration or deceleration. This presents a difficulty in directly calculating the boundary layer height.

To calculate T, we base our approach on the observation that vorticity outside of an attached boundary layer is negligible. Since the boundary layers have the largest velocity gradients very close to the wall, vorticity here is the highest and decreases as one moves farther away from the wall. As boundary layer growth curves are in most cases perpendicular to the wall, one can walk along these edges starting from the wall, and determine the point at which the vorticity drops below a threshold value. This threshold value depends on the local maximum value of vorticity for attached boundary layers, which is most often encountered at the wall. Through our analysis, we have found that a good value for the threshold is 0.02% of the wall vorticity magnitude.

E. Growth factor (r) and number of layers (n)

To increase the boundary layer elements' height away from the wall, a growth factor (also called as the stretching factor) greater than 1 is used. This is because the tightest mesh spacing is required very close to the wall, but this requirement is not as strict further away. An ideal scenario would be to achieve height of the last layer equal to the unstructured sizes of the mesh and get a smooth transition. The mesh adaptation process provides options like boundary layer gradation factor, which control the transition of boundary layer into the unstructured part of the mesh, smoothly.[16]

There are general guidelines for what the ideal growth factor should be, from the perspective of turbulence modeling. Spalart[17,18] states that the growth factor should be close to 1.25 to accurately capture the log layer. Generally a growth factor beyond the value of 1.4 is deemed too large for accurately capturing the boundary layers. Many meshing tools are based on setting t_o, T and n, and the growth factor is automatically calculated, internally. The accuracy then in turn hinges on the knowledge and prior calculation to make sure that the growth factor being calculated is acceptable.

The adaptation tool gives the ability to set the growth factor at each wall vertex. We set r in the range of 1.2-1.25 to be within the acceptable limits. Selecting a growth factor less than 1.2 has the disadvantage of more elements in the boundary layer than needed. The number of layers are then calculated using eq.1.

F. Handling the separated boundary layers

The techniques described above for calculating the different aspects of the boundary layer meshes work well for attached boundary layers. However, separated boundary layers need extra care and special detection strategies due to different flow physics that must be captured.

1. *Detection of separated boundary layers*

To treat separated boundary layers properly, they must first be detected. As it can be seen from fig. 6, they have a unique profile characterized by flow reversal. We again make use of the wall normal growth curves and walk along the growth edges to detect a change in the flow direction. If a change (usually more than 120^o) is detected across the profile, then the vertex on the wall is marked as *separated*; otherwise the boundary layer is treated as an attached boundary layer.

This method requires that the total height of the mesh boundary layers in this region at least exceeds the height at which the flow direction is reversed. This means that typically initial boundary layer meshes for such regions should be tall enough and mesh very close to the wall wall be fine enough to capture the flow reversal. Currently we make sure that this criteria is satisfied through initial meshing, but an iterative adaptive procedure like the one we use eventually leads to suitable meshes which are able to capture this effect.

2. Calculation of the wall shear stress

The method of using Spalding's law to calculate the wall shear stress, is not appropriate for separated boundary layers, since the typical turbulent profile is absent. In such a case, where separation is detected, wall shear stress is calculated using the finite difference method explained earlier. The accuracy of such calculations is not as good as other methods, but it gives a reasonable estimate. Also, for separated boundary layers, the first cell height of the mesh boundary layer is not as crucial as for the attached boundary layers, hence such an approximate approach is justifiable.

3. Total height of the boundary layer (T)

For separated boundary layers, the free shear layer might get separated from the wall to a fair distance, in which case it might not be prudent to increase the boundary layer height. Even though it would be a good feature to separate the mesh boundary layer from the wall to resolve the free shear layer, this capacity is still under development with the current adaptive tools that we use.

The techniques explained above for attached boundary layers predict that the boundary layer's height should be increased to the height of the complete shear layer. However, this is not always practical for separated boundary layers as this height might introduce excessive stretching of the elements near the interface.

In a more practical approach, the boundary layer height is increased beyond the height at which the flow reversal is detected so that the boundary layer mesh is tall enough to "sense" the change in the flow direction and the rest of the boundary layer mesh is destroyed and the free shear layer region is meshed with unstructured elements, with specific care to resolve the free shear layer. This approach is used in this work. For anisotropic adaptivity, velocity Hessians give good resolution in these layers since the anisotropy of the top of the shear layer is not very high.

G. Shock wave - boundary layer interactions

In transonic and supersonic flows, the main region of interest is where the shock waves and the boundary layers interact. Shock waves are sharp discontinuities in the flow and can cause thickening of the boundary layer and even separation. Due to their complex nature, these regions need greater attention and higher resolution. Since the in-plane mesh sizes for the shock wave - boundary layer interactions are smaller, care needs to be taken to trim away the boundary layer elements that develop anisotropy in the wrong direction as the in-plane resolution becomes finer than the normal direction resolution. One way to control this, is by limiting the mesh boundary layer height.

When the flow encounters a shock, the solution changes sharply, giving high gradients in this region. We implemented a shock wave - boundary layer detection algorithm which detects a shock-boundary layer interaction by looking at the pressure gradients on the wall. If such a region is detected, then the wall vertices are marked to not increase the boundary layer height beyond a certain limit to avoid poorly shaped boundary layer elements. The boundary layer height in the shock region is limited by a factor of the upstream boundary layer height, so that it does not change suddenly with the shock.

IV. Results

In this section we present two transonic flow applications of our adaptive boundary layer meshing techniques.

A. Delery Bump

The first case that we used for analysis is the Delery bump, which is a 2D bump with steady transonic flow. This case is often used to evaluate the performance of turbulence models. Air enters the nozzle from a reservoir at $p_t = 96000\,Pa$ and $T_t = 300\,K$, and accelerates over the bump reaching supersonic speeds. The exit pressure is maintained at $61500\,Pa$. For these inlet and exit pressures, the flow develops a shock on the leeward side of the bump. The experiments for this case were first carried out by Delery.[19]

The PHASTA compressible finite element flow solver was used for the simulations. We used RANS Spalart-Allmaras one equation turbulence model[14] in this study. The adaptivity used combined pressure and velocity Hessians as error indicators.[4] The first cell height is requested at $y^+ = 1$. Because the flow separates after the shock, separation detection algorithm detects the region and the boundary layer attributes are set accordingly.

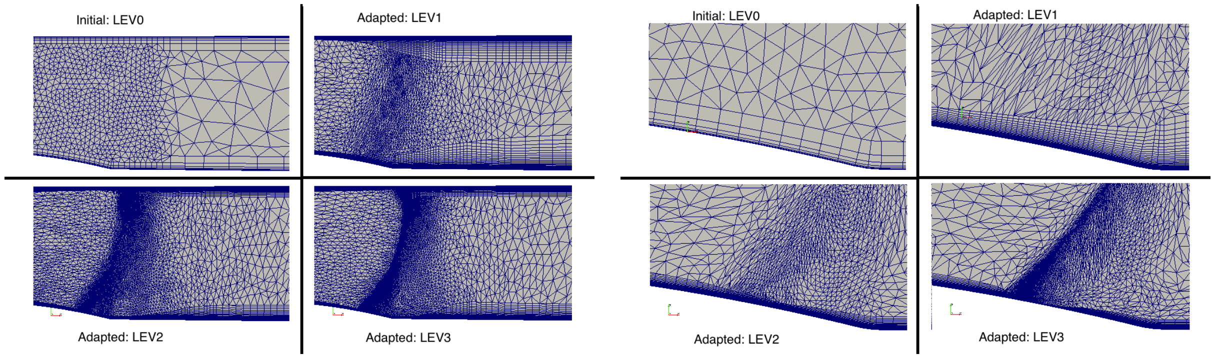

(a) Initial and adapted meshes (b) Zooms of the shock wave - boundary layer interaction zone

Figure 7. initial and adapted meshes for the Delery bump

Fig. 7(a) shows zooms of the initial and the adapted meshes over the bump. The boundary layer thickens after the shock as expected. Before the shock, boundary layer thickness remains low on both the bottom and the top walls. In the separated region, the boundary layer height is maintained until the flow reversal is detected in the boundary layer profile. The LEV1 mesh shows some overshoot in the boundary layer thickness, but latter adapted meshes show converged behavior in terms of the boundary layer height. Adaptive refinement follows the curved shock such that the direction normal to the shock is refined much more than along the shock. This behavior is more evident from fig. 7(b), which displays the meshes in the shock wave - boundary layer interaction region. The adapted LEV2 and LEV3 meshes knock down the boundary layer height in the vicinity of the shock which is in accordance to the shock detection algorithm. One thing to notice is that the initial mesh is too coarse to detect the flow reversal which occurs immediately after the shock and the boundary layer height is maintained according to the attached boundary layer algorithm. However, the adapted LEV1 mesh becomes fine enough to detect the profile change and separation is detected and the boundary layer is destroyed immediately after the shock and is maintained only until the height at which flow reversal is detected.

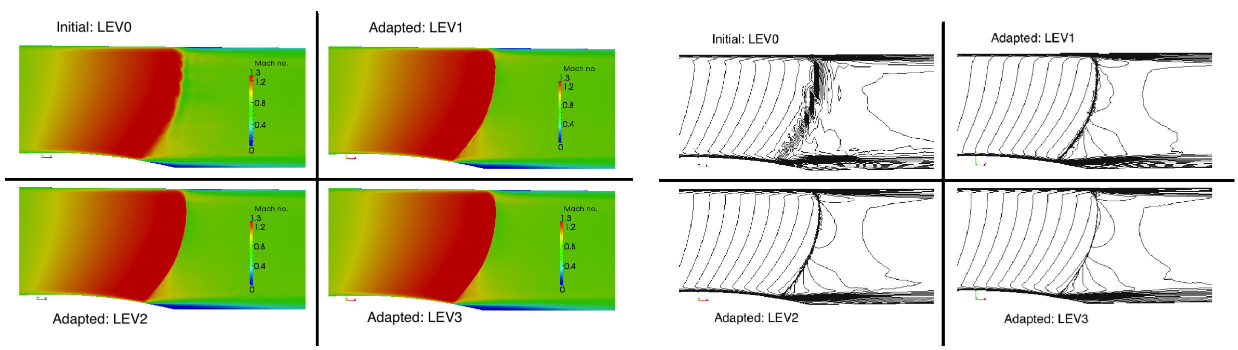

(a) Mach number for a slice along the symmetry plane (b) Mach number contours

Figure 8. Mach number slice and contours for the Delery bump

Fig. 8 shows slices of Mach number and Mach number contours. The contours show progressive sharpness in the shock region, with adaptivity. The LEV3 mesh gives the sharpest resolution of the contours. A weak vertical shock is seen in fig. 8(a), originating from the intersection of the curved and the straight section of the strong shock.

Fig. 9(a) shows pressure slice for the shock region over the bump. The adapted meshes are able to resolve the shock sharply as compared to the initial mesh; the best resolution is given by the LEV3 mesh. Fig. 9(b) shows a zoom of the shock wave - boundary layer interaction zone and streamlines in the separation zone after the shock. The location of the interaction zone is better predicted in the adapted meshes and moves a bit to the right with respect to the initial mesh. The initial mesh over predicts the size of the the separation bubble, which gets corrected in the adapted meshes. The LEV2 and LEV3 meshes show similar behavior of the streamlines, indicating converged behavior of the separation bubble.

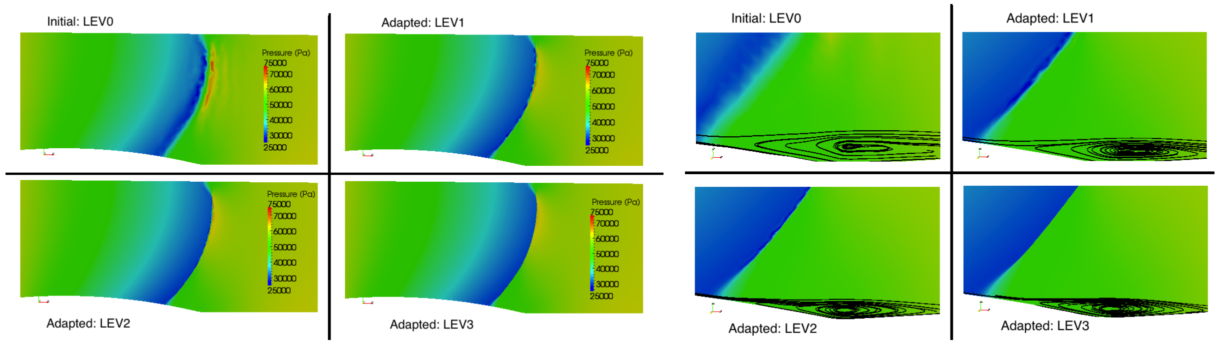

(a) Pressure (b) Streamlines in the separation zone

Figure 9. Pressure slice along the symmetry plane, with a zoom of the shock-BL interaction zone and the separation bubble

	Separation point (x/h)	Reattachment point (x/h)
Initial mesh (LEV0)	22.33	26.60
Adapted mesh (LEV1)	22.08	26.66
Adapted mesh (LEV2)	22.15	27.08
Adapted mesh (LEV3)	22.14	27.16
Experiments (Delery[19])	21.84	27.04

Table 1. Separation and reattachment locations for the Delery bump, normalized by the bump height

Table 1 lists the separation and reattachment points for different meshes. The distance values are normalized by the height of the bump (h), which is $12mm$. The initial mesh predicts delayed separation and earlier reattachment than the experiment values. The adapted meshes, especially LEV2 and LEV3, give a better agreement with the experimental results.

The normalized bottom wall pressure is plotted in fig. 10 and indicates good agreement between the experimental and the simulation values for initial and adapted meshes. The flow solver over predicts the wall pressure after the shock, in the separation zone. This behavior has been seen before by Emory et. al[20] and Lien et al.[21] These differences can be attributed to the three dimensional nature of the experiment and to the turbulence model's limitations in capturing the effect of separation, and so it is not a concern of this paper.

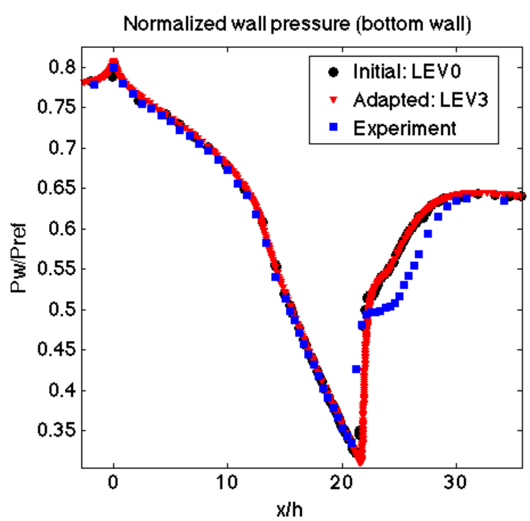

Figure 10. Normalized bottom wall pressure for the Delery bump

Boundary layer profiles are plotted in fig. 11 along various stream-wise locations. Figure 11(a) and 11(b) show boundary layer profiles in the separation zone after the shock. The initial mesh is not able to capture the correct behavior due to its coarse resolution in this region. The adapted LEV3 mesh shows much better agreement with the experimental values in the separation zone. This is particularly important because in the separation zone, we are limiting the height of the mesh boundary layers. For the boundary layer profiles after reattachment shown in fig. 11(c) and 11(d), adapted and initial meshes both give good approximations to the profile.

To make sure grid convergence was reached, we uniformly refined the LEV3 mesh. This means that each mesh edge was split into two to get a new LEV4 mesh. This LEV4 mesh showed no difference in the solution

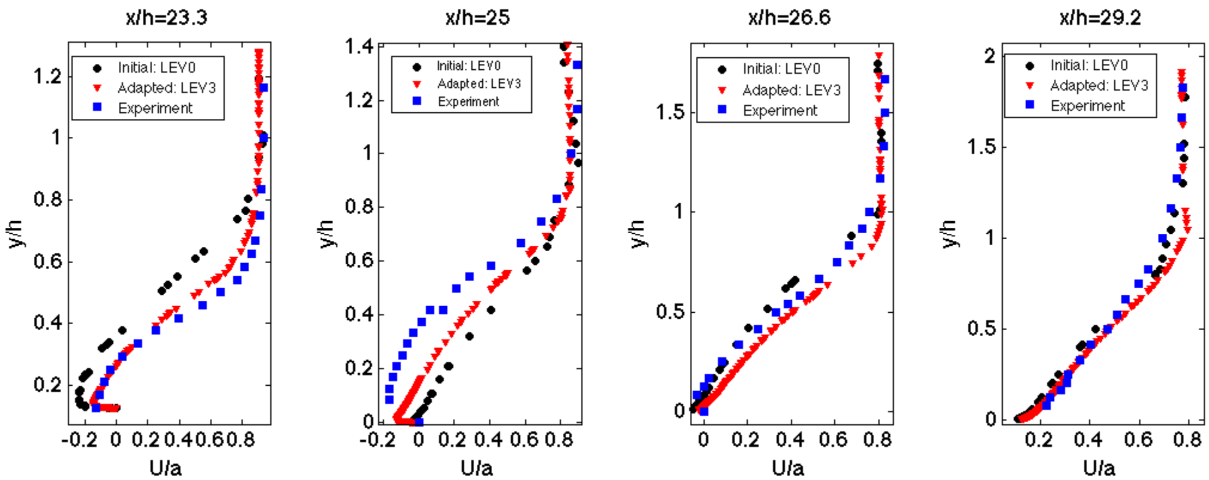

(a) x/h = 23.3 (b) x/h = 25 (c) x/h=26.6 (d) x/h=29.2

Figure 11. Boundary layer profiles at various stream-wise sections for the Delery bump

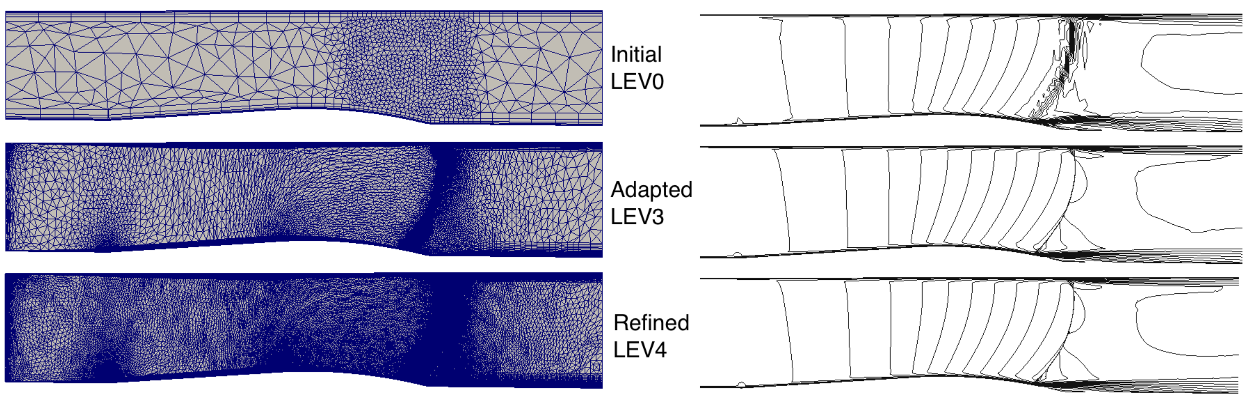

Figure 12. Initial LEV0, adapted LEV3 and uniformly refined LEV4 meshes and corresponding Mach number contours for the Delery bump case

when compared to the LEV3 mesh, which makes a strong case for verification of the results. Fig. 12 shows the LEV4 mesh generated with uniform refinement in comparison to the initial LEV0 and the adapted LEV3 mesh. The mach contours on the right show no significant difference in their behavior, displaying that grid independence is reached. This means that any further mesh refinement beyond the LEV3 mesh produces the same result and is redundant.

B. ONERA M6 wing

The ONERA M6 wing is a classic CFD validation case. Air enters the wind tunnel at transonic speed and is accelerated over the wing to supersonic speeds causing a shock to appear on the upper surface of the wing. The free stream Mach number is 0.84, and the angle of attack is 3.06^o. The free stream pressure and temperature are 42.89 psi and 255.5 K. The Reynolds number is 11.72 Million based on the mean aerodynamic chord. This flow marks a strong need for adaptive grids due to its unknown shock location *a priori* to the flow solve and complex nature of the lambda shock. The reference experimental data is from Schmitt and Charpin, 1979.[22]

We used Spalart Allmaras one equation turbulence model for this case.[14] Pressure Hessians were used as error indicators to resolve the shock on the wing surface. The first cell height was requested at $y^+ = 1$.

Fig. 13 shows the initial and the adapted meshes for the wing and corresponding surface pressure contours, on the left side. The mesh gets refined in the shock region and the lambda shape of the shock is clearly replicated in the mesh. The mesh downstream of the shock is coarsened, due to low values of pressure

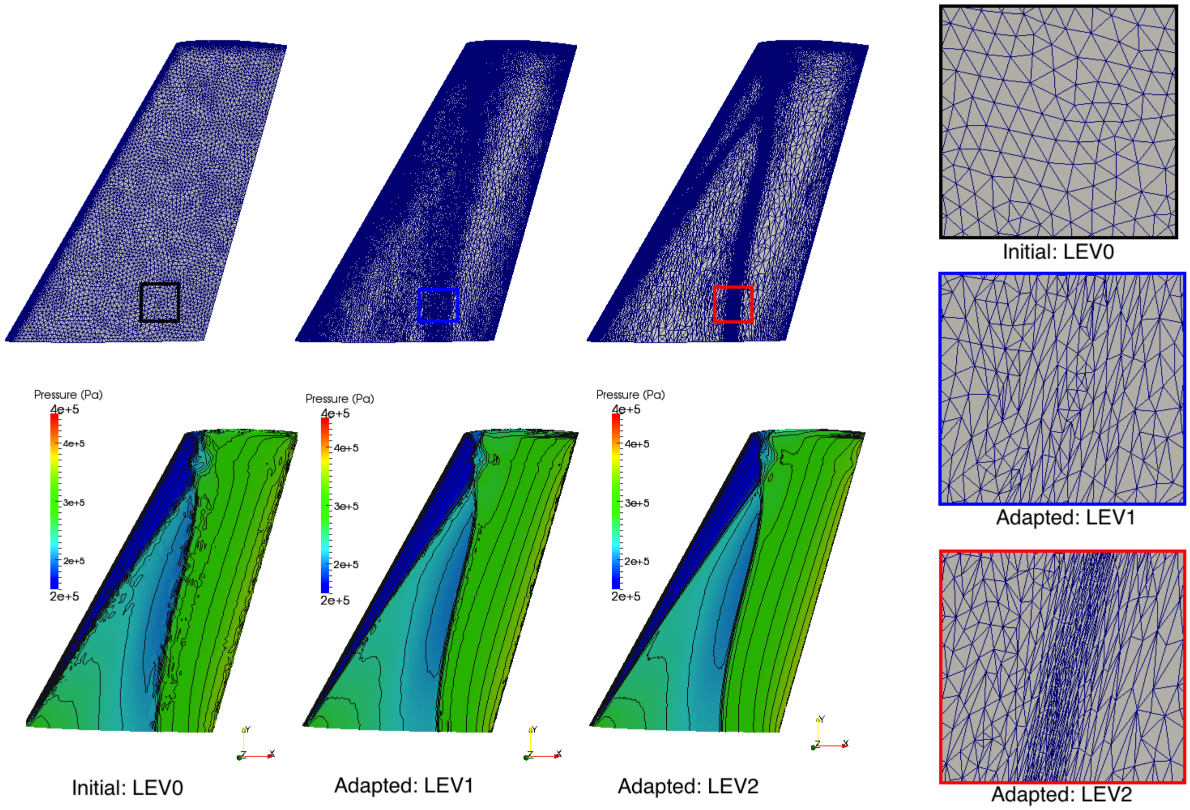

Figure 13. Meshes and corresponding surface pressure plots and contours

gradients in this region. The surface pressure contours become sharper and more regular in shape with adaptivity. On the right hand side of fig. 13, the pictures show the zooms of the shock region on the wing, displaying the anisotropy developed in the surface elements along the shock as compared to the direction normal to the shock. One thing to notice is that the elements start aligning themselves with the shock in adapted LEV1 mesh, but need one more adaptation loop to completely show this behavior in a satisfactory manner.

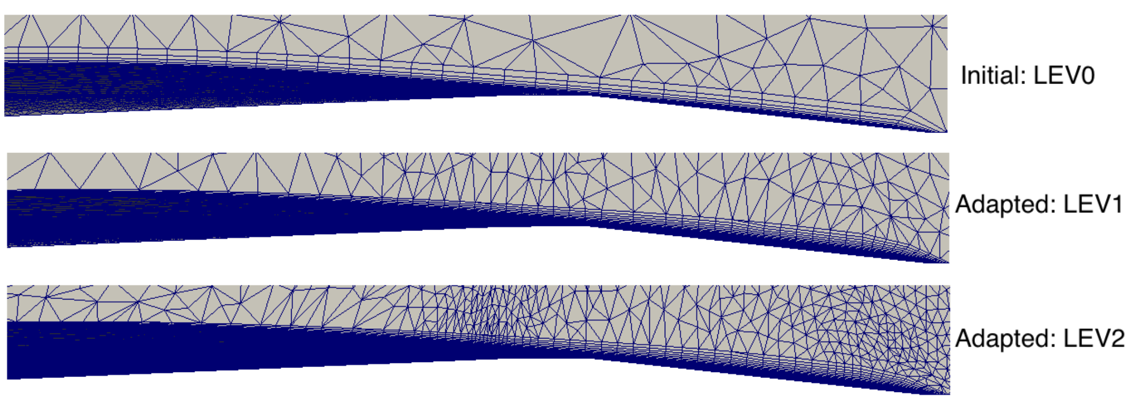

Figure 14. Change in the boundary layer height on upper surface of the wing

To illustrate the changing attributes of the mesh boundary layer with adaptivity, fig. 14 shows the boundary layer on the upper surfaces of the wing for the initial and the adapted meshes. Clearly, the boundary layer prior to the shock remains relatively low in total height. After the shock the boundary layer thickens as expected. The zone where shock wave meets the boundary layer can also be seen and the elements oriented with finer resolution normal to the shock and longer edges along the shock are clearly visible.

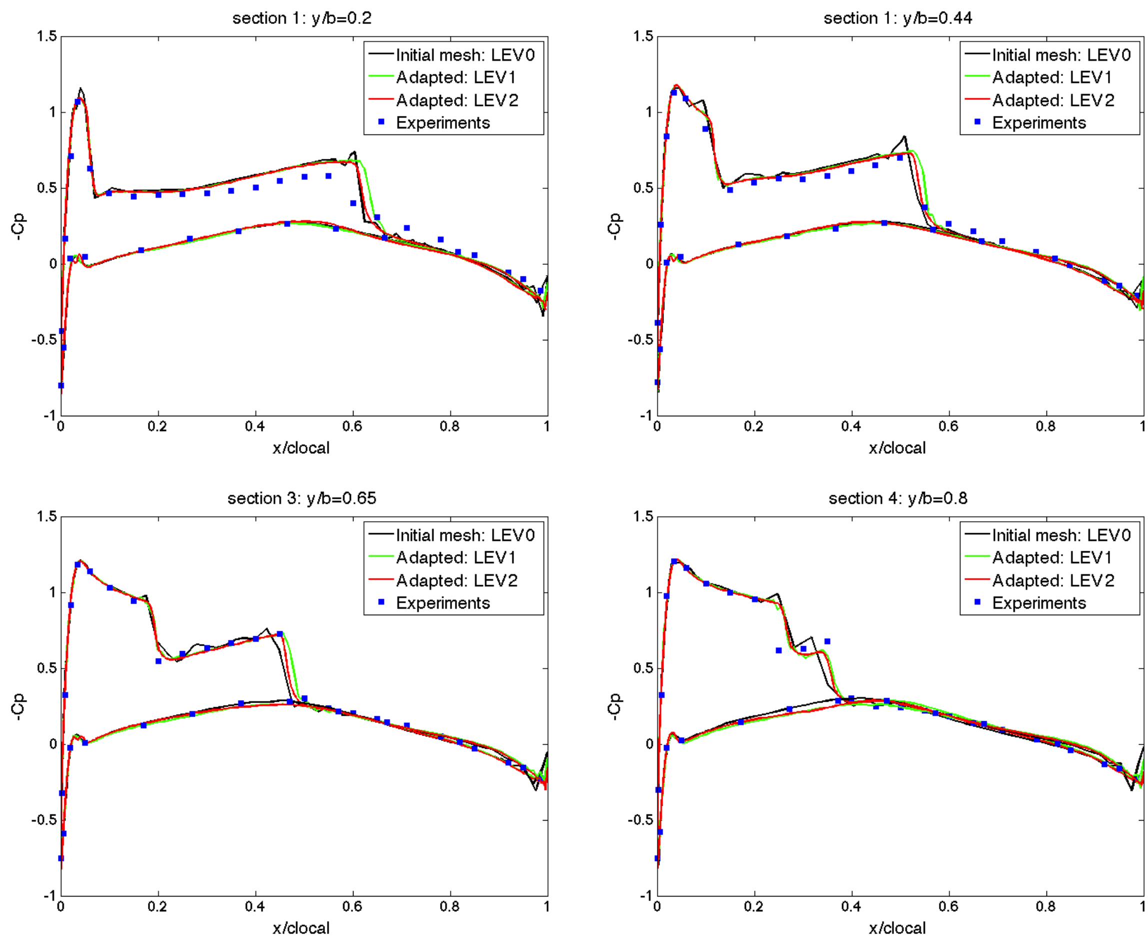

Figure 15. Coefficient of pressure on the wing at various spanwise sections

Fig. 15 shows coefficient of pressure plots for different span-wise sections of the wing. The initial mesh shows some overshoot near the shock which is expected due to its coarse nature. Adaptivity removes this problem and gives C_p values which match the experimental data. One particular area of interest is the shock on section 4 ($y/b = 0.8$), which is in fact a double shock. PHASTA is able to capture this double discontinuity and adaptivity improves the agreement with the experiments in this region.

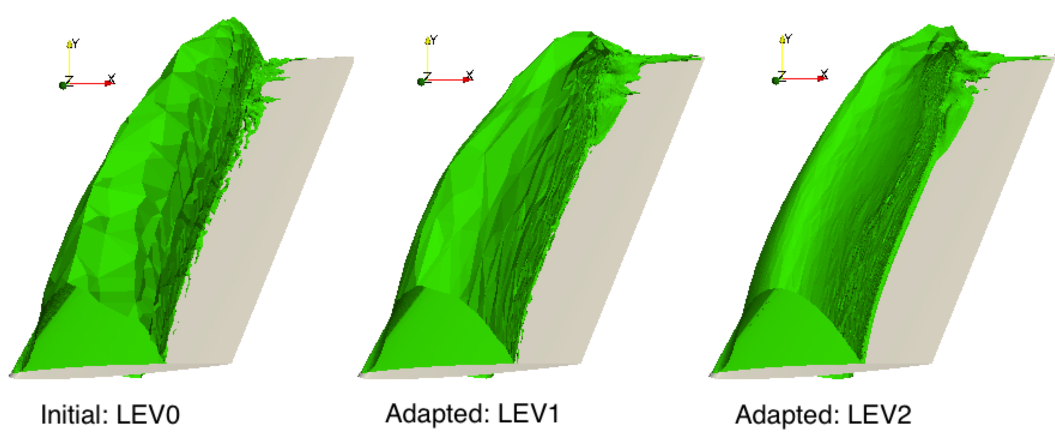

Figure 16. Iso-surface of Mach 1 for initial and adapted meshes

Fig. 16 shows iso-surfaces of Mach number equal to unity on the upper surface of the wing. The anisotropy developed in the spanwise direction is replicated on the iso-surfaces. In general, the adapted meshes show smoother curves indicating higher degree of resolution as compared to the initial mesh.

Overall, for ONERA M6 wing case we see that the adapted meshes were able to capture the shock with higher accuracy than the initial mesh. The C_p values agree well with the experiments and improve with adaptivity.

V. Conclusion

In this paper we have presented anisotropic adaptive boundary layer meshes and their application to transonic turbulent flows. A new way to adaptively calculate the attributes of boundary layer meshes is described and is combined with the traditional numerical error indicators to drive overall mesh adaptivity. A clear advantage of such an approach is the use of flow physics to set normal mesh spacings near the walls, instead of using less effective error indicators.

We demonstrated the ability of this approach to capture the boundary layer physics as well as other flow regions by applying the adaptive techniques to two transonic flow cases. The first application was the Delery bump, where adaptivity improved the shock resolution and the boundary layer profiles. The separation zone was captured with greater accuracy with adaptivity. A uniform refinement of the adapted mesh was used to verify the adaptivity approach arrived at a grid independent solution. The second application was ONERA M6 wing, where adaptivity helped to get better results in terms of the surface pressure contours and the coefficient of pressure on the wing. We also showed that the shock wave-boundary layer interactions are captured better with adaptive boundary layer meshes.

Acknowledgments

The work was carried out at University of Colorado Boulder, in partnership with Simmetrix, Inc. and Rensselaer Polytechnic Institute, and was supported a NASA STTR.

This work utilized the Janus supercomputer, which is supported by the National Science Foundation (award number CNS-0821794) and the University of Colorado Boulder. The Janus supercomputer is a joint effort of the University of Colorado Boulder, the University of Colorado Denver and the National Center for Atmospheric Research.

References

[1]Pirzadeh, S., "Unstructured viscous grid generation by advancing-layers method," *AIAA J.*, Vol. 32, 1994, pp. 1735–1737.

[2]Garimella, R. V. and Shephard, M. S., "Boundary layer mesh generation for viscous flow simulations," *Int. J. Numer. Meth. Eng.*, Vol. 49, 2000, pp. 193–218.

[3]Sahni, O., Jansen, K. E., Shephard, M. S., Taylor, C. A., and Beall, M. W., "Adaptive boundary layer meshing for viscous flow simulations," *Engineering with Computers*, Vol. 24(3), 2008, pp. 267–285.

[4]Ovcharenko, A., Chitale, K., Sahni, O., Jansen, K. E., and Shephard, M., "Parallel anisotropic mesh adaptation with boundary layers," *Proceedings of the 21st International Meshing Roundtable*, 82, IMR, 2012, pp. 437–455.

[5]Jansen, K. E., "Unstructured grid large eddy simulations of wall bounded flows," *Annual Research Briefs,*, Center for Turbulence Research, NASA Ames/Stanford University, 1993, pp. 151–156.

[6]Jansen, K. E., "Unstructured grid large eddy simulations of flow over an airfoil," *Annual Research Briefs*, Center for Turbulence Research, NASA Ames/Stanford University, 1994, pp. 161–173.

[7]Jansen, K. E., Johan, Z., and Hughes, T. J. R., "Implementation of one-equation turbulence model within a stabilized finite element formulation of a symmetric advective-diffusive system," *Comp. Meth. Appl. Mech. Eng.*, Vol. 105, 1993, pp. 405–433.

[8]Shur, M. L., Spalart, P. R., Strelets, M. K., and Travin, A. K., "A hybrid RANS-LES approach with delayed-DES and wall-modeled LES capabilities," *Int. J. of Heat and Fluid Flow.*, Vol. 29, 2008, pp. 1638–1649.

[9]Buscaglia, G. C. and Dari, E. A., "Anisotropic mesh optimization and its application in adaptivity," *Int. J. of Numer. Meth. Eng.*, Vol. 40, 1997, pp. 4119–4136.

[10]Casto-Diaz, M. J., Hecht, F., Mohammadi, B., and Pironneau, O., "Anisotropic unstructured mesh adaptation for flow simulations," *Int. J. Numer. Meth. Fluids*, Vol. 25, 1997, pp. 475–491.

[11]Li, X., Shephard, M. S., and Beall, M. W., "3D anisotropic mesh adaptation by mesh modifications," *Comp. Meth. Appl. Mech. Eng.*, Vol. 194, 2005, pp. 4915–4950.

[12]Apel, T. and Dobrowolski, M., "Anisotropic interpolation with applications to the finite element method," *Computing.*, Vol. 47, 1992, pp. 277–293.

[13]Sahni, O., Muller, J., Jansen, K. E., Shephard, M. S., and Taylor, C. A., "Efficient anisotropic adaptive discretization of the cardiovascular system," *Comp. Meth. Appl. Mech. Eng.*, Vol. 195, 2006, pp. 5634–5655.

[14]Spalart, P. R. and Allmaras, S. R., "A one-equation turbulence model for aerodynamic flows," *AIAA paper 92–439*, 1992.

[15]Spalding, D. B., "A single formula for the law of the wall," *J. Appl. Mech.*, Vol. 28, 1961, pp. 455–458.

[16]Li, X., Remacle, J. F., Chevaugeon, N., and Shephard, M. S., "Anisotropic mesh gradation control," *13th International Meshing Roundtable*, 2004, pp. 401–412.

[17]Spalart, P. R., "Trends in turbulence treatments," *AIAA 2000-2306*, June 2000.

[18]Spalart, P. R., "Young-person's guide to detached-eddy simulation grids," *NASA/CR-2001-211032*, National Aeronautics and Space Administration, 2001.

[19]Delery, J. M., "Investigation of strong shock turbulent boundary layer interaction in 2-D transonic flows with emphasis on turbulence phenomena," *Proceedings of 14th Fluid and Plasma Dynamics conference*, American Institute of Aeronautics and Astronautics, 1981.

[20]Len, F. S. and Kalitzin, G., "Computations of transonic flow with $v^2 - f$ turbulence model," *International Journal of Heat and Fluid Flow*, Vol. 22, 2001, pp. 53–61.

[21]Emory, M., Pecnik, R., and Laccarino, G., "Modeling structural uncertainties in Reynolds-averaged computations of shock/boundary layer interactions," *AIAA 2011-0479*, 2011.

[22]V. Schmitt and F. Charpin, "Pressure distribution on the ONERA-M6-Wing at transonic mach numbers," *Report of the Fluid Dynamics Panel Working Group 04*, Vol. 138, AGARD, May 1979.